

Infinitely adaptive transition metal oxychalcogenides: the modulated structures of $\text{Ce}_2\text{O}_2\text{MnSe}_2$ and $(\text{Ce}_{0.78}\text{La}_{0.22})_2\text{O}_2\text{MnSe}_2$

Chun-Hai Wang^(a), Chris M. Ainsworth^(a), Dong-Yun Gui^(a), Emma E. McCabe^(a, c), Matthew G. Tucker^(b), Ivana R. Evans^(a, d) and John S. O. Evans^{(a, d)*}

^(a)Department of Chemistry, University Science Site, Durham University, South Road, Durham, DH1 3LE, United Kingdom

^(b)ISIS Neutron and Muon Source, Science and Technology Facilities Council, Rutherford Appleton Laboratory, Harwell, Oxford, Didcot, UK, OX11 0QX

^(c)School of Physical Sciences, University of Kent, Canterbury CT2 7NH, United Kingdom

^(d)The Bragg Institute, ANSTO (Australian Nuclear Science and Technology Organisation), New Illawarra Road, Rutherford Avenue, Lucas Heights, NSW 2234, Australia.

Keywords: layered oxychalcogenide, modulated structure, (3+1)D superspace, magnetic structures

ABSTRACT: This paper reports the synthesis, structures and physical properties of the oxychalcogenides $(\text{Ce}_{1-x}\text{La}_x)_2\text{O}_2\text{MnSe}_2$ with $x = 0 - 0.7$. These materials have a layered structure related to that of the LaOFeAs -derived superconductors, but with the transition metal sites 50% occupied. $\text{Ce}_2\text{O}_2\text{MnSe}_2$ contains alternating layers of composition $[\text{Ce}_2\text{O}_2]^{2+}$ and $[\text{MnSe}_2]^{2-}$. The size mismatch between the layers leads to an incommensurate structure with a modulation vector of $\mathbf{q} = \alpha\mathbf{a}^* + \mathbf{0b}^* + 0.5\mathbf{c}^*$ with $\alpha = 0.158(1)$, which can be described with a (3+1)D superspace structural model in superspace group $Cmme(\alpha\mathbf{0}\frac{1}{2})\text{oso}$ [67.12]. There is a strong modulation of Mn site occupancies leading to a mixture of corner- and edge-sharing $\text{MnSe}_{4/2}$ tetrahedra in the $[\text{MnSe}_2]^{2-}$ layers. The modulation vector can be controlled by partial substitution of Ce^{3+} for larger La^{3+} and a simple commensurate case was obtained for $(\text{Ce}_{0.78}\text{La}_{0.22})_2\text{O}_2\text{MnSe}_2$ with $\alpha = 1/6$. The materials respond to the change in relative size of the oxide and chalcogenide blocks by varying the ratio of corner- to edge- sharing tetrahedra. The superspace model lets us unify the structural description of the five different ordering patterns reported to date for different $\text{Ln}_2\text{O}_2\text{MSe}_2$ ($\text{Ln}=\text{lanthanide}$) materials. Mn moments in $\text{Ce}_2\text{O}_2\text{MnSe}_2$ and $(\text{Ce}_{0.78}\text{La}_{0.22})_2\text{O}_2\text{MnSe}_2$ order antiferromagnetically below $T_N = 150$ K and Ce moments order below ~ 70 K. The magnetic structures of both materials have been determined using neutron diffraction. Both materials are semiconductors; $\text{Ce}_2\text{O}_2\text{MnSe}_2$ has $\sigma = 9 \times 10^{-6} \Omega^{-1}\text{cm}^{-1}$ at room temperature and an activation energy for charge carrier mobility from RT to 170°C of ~ 0.4 eV.

INTRODUCTION

Inorganic materials built from the stacking of well-defined sublayers form a large, diverse and technologically important family. Exploitable behaviour exhibited by such layered systems includes high-temperature superconductivity,¹⁻³ magnetic properties,^{4,5} ionic conductivity,⁶⁻⁹ optical¹⁰ and thermoelectric properties.¹¹⁻¹³ Layered structures are particularly prevalent amongst mixed anion systems as they can provide a natural way to simultaneously satisfy the bonding requirements of hard and soft cations in the presence of hard and soft anions. For example, there are many layered oxychalcogenides and oxypnictides which contain oxide blocks separated by chalcogenide (S, Se, Te) or pnictide (P, As, Sb, Bi) blocks¹⁴. Perhaps the most famous are the F-doped LnOFeAs ($\text{Ln} = \text{lanthanide}$) oxypnictides which have the ZrCuSiAs -type structure and show superconductivity at temperatures up to 55 K.^{2,14,15} The

structure of these materials can be described as 2D layers of edge-sharing fluorite-like $\text{OLn}_{4/4}$ tetrahedral layers alternating with edge-sharing $\text{FeAs}_{4/4}$ anti-fluorite tetrahedral layers (Figure 1).¹ Ln ions bond to both O^{2-} and As^{3-} layers in a 4O+4As distorted square antiprismatic coordination environment. The ZrCuSiAs -type layered structure is also found for the Cu^+ -containing oxychalcogenides LnOCuCh ($\text{Ln} = \text{Y, La} - \text{Nd}$; $\text{Ch} = \text{S, Se}$).¹⁶⁻²⁰ When Cu^+ ions in the Cu-Se layers of LnOCuSe are replaced by divalent metal cations M^{2+} , layered structures of composition $\text{LnOM}_{0.5}\text{Se}$ (or $\text{Ln}_2\text{O}_2\text{MSe}_2$) may be formed in which only half of the tetrahedral sites in the selenide layer are occupied. Before this work, six different layered $\text{Ln}_2\text{O}_2\text{MSe}_2$ materials had been reported: $\text{Ce}_2\text{O}_2\text{MnSe}_2$

ⁱ $\text{AX}_{4/4}$ indicates each X of an AX_4 tetrahedron is shared by 4 other tetrahedra.

(CeOMn_{0.5}Se)²¹, La₂O₂CdSe₂,²²⁻²⁴ Ce₂O₂FeSe₂,²⁵ La₂O₂FeSe₂,²⁶ La₂O₂ZnSe₂,²⁷ and Ce₂O₂ZnSe₂.²⁸ The difference between their structures is the ordering patterns of the M²⁺ sites, as shown in Figure 1. In Ce₂O₂MnSe₂ (CeOMn_{0.5}Se), Mn²⁺ has been reported to half occupy tetrahedral sites randomly giving a structure with symmetry *P4/nmm* (No. 129).²¹ In La₂O₂CdSe₂, the Cd²⁺ occupies alternate tetrahedral sites in an ordered pattern forming a checkerboard-like array with

space group *P4₂/nmc* (137).²³ In Ce₂O₂FeSe₂ and La₂O₂FeSe₂, Fe²⁺ orders in a different way to form a stripe-like pattern^{25,26} with space group *Imcb* (72). The Zn ordering pattern in La₂O₂ZnSe₂ contains a mixture of corner- and edge-sharing tetrahedra (ratio 3:1) with space group *Cmca* (64).²⁷ Ce₂O₂ZnSe₂²⁸ shows a similar ordering pattern to La₂O₂ZnSe₂, but with a ratio of corner- to edge-sharing tetrahedra of 4:1 and space group *Imcb*.

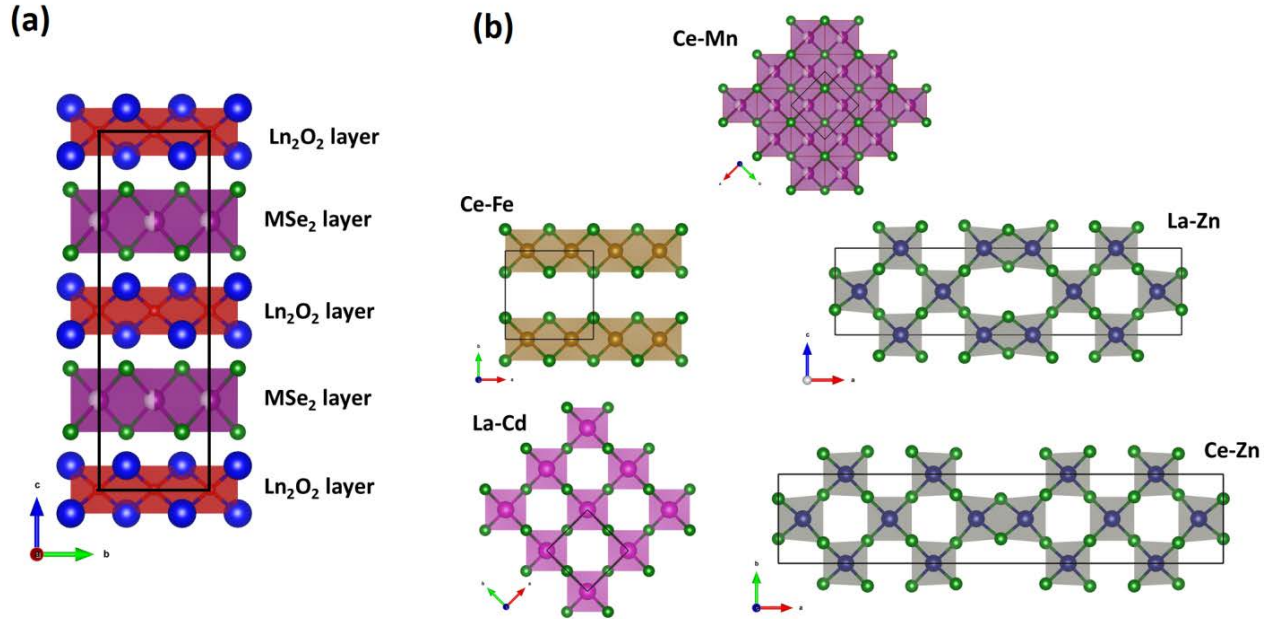


Figure 1. ZrCuSiAs parent structure of layered Ln₂O₂MSe₂ phases.^{21,23,25,27,28} (a) General side view; (b) Ordering patterns of MSe_{4/2} layer for different Ln-M systems. Alternate MSe_{4/2} layers are out of phase in terms of M site occupancies. Blue = Ln, red = O, green = Se, other colours = M.

Our recent work on Ln₂O₂MSe₂ systems has led us to reinvestigate the disordered structural model of Ce₂O₂MnSe₂ reported by Ijjaali *et al.*²¹ and we observe features in the diffraction data of both powdered and single crystal samples that can't be explained by their model. Based on our data, we propose an incommensurately modulated structure model for Ce₂O₂MnSe₂. Understanding this structure has allowed us to prepare the simple commensurate material (Ce_{0.78}La_{0.22})₂O₂MnSe₂. The structures of both these materials are reported along with their conductivity and magnetic structures and properties. Based on these observations we propose a unifying structural model to describe all the layered Ln₂O₂MSe₂ materials reported to date and show that they should be considered as a new infinitely adaptive structure type.

EXPERIMENTAL DETAILS

Synthesis. Polycrystalline samples of Ce₂O₂MnSe₂ and (Ce_{1-x}La_x)₂O₂MnSe₂ were prepared by solid state reaction. CeO₂ (99.99%, Alfa Aesar), La₂O₃ (99.99%, Aldrich, heated at 1000 °C before use), Se (99.999%, Alfa Aesar), and Mn (99.9%, Koch-Light) were selected as raw materials. Stoichiometric amounts were weighed and ground in an agate mortar and pestle. The well-mixed powders were placed into an alumina

crucible and sealed with a second alumina crucible filled with Ti (99.5%, Alfa Aesar, 5% molar excess) powder acting as oxygen getter (forming TiO₂) in a silica tube. The tubes were evacuated to < 10⁻² mbar before sealing. The sealed tubes were heated slowly to 600 °C for 24 h and 1000 °C for 48 h. After cooling, the samples were ground, resealed in silica tubes, and reheated at 1000 °C for 48 h.

For preparation of Ce₂O₂MnSe₂ single crystals, stoichiometric amounts of CeO₂, Mn, Se, and KCl flux (99%, Alfa Aesar, heated to 150 °C before use) were weighed and ground. The amount of KCl was ca. 10 times the molar amount of Ce₂O₂MnSe₂. The mixture was placed into an alumina crucible and sealed with another alumina crucible filled with Ti (5% molar excess) powder. The tube was then heated to 600 °C at 60 °C/h, held for 24 h; heated to 950 °C at 60 °C/h, held for 96 h, ramped to 850 °C at 60 °C/h and held for 96 h, cooled to 600 °C at 2 °C/h and finally to room temperature at 100 °C/h. The reacted mixture was washed with water to remove KCl and dried with acetone. Using polarised microscopy, dark orange single crystal plates were observed.

Powder X-ray diffraction (PXRD). PXRD data for Ce₂O₂MnSe₂ and (Ce_{1-x}La_x)₂O₂MnSe₂ were collected at room temperature (RT) from 5 - 140° 2θ in reflection mode using a Bruker D8 powder diffractometer on samples sprinkled on

zero-background Si wafers. Cu K α radiation (tube condition: 50 kV, 40 mA), variable divergence slits and a Lynxeye Si strip position detector (PSD) were used. For Rietveld-quality data a scan step of 0.01° and scan time of ca. 15 h were used. To determine modulation vectors in the (Ce_{1-x}La_x)₂O₂MnSe₂ solid solution, a ca. 1h scan with 0.02°/step was used. Variable temperature PXRD data (~2 K intervals, 20 minutes scans) on Ce₂O₂MnSe₂ were recorded from 13 K to 300 K (warming). The temperature was controlled by an Oxford Cryosystems Phenix cryostat.

Single crystal X-ray diffraction (SXRD). SXRD data of Ce₂O₂MnSe₂ (~ 0.12 mm × 0.15 mm × 0.04 mm) were collected using a Bruker D8 VENTURE single crystal diffractometer at room temperature. An I μ S Microfocus Source Mo radiation (50 kV, 1 μ A) and PHOTON 100 CMOS detector were used. A total of 1020 frames were recorded at 7 s/frame.

Selected area electron diffraction (SAED). SAED patterns of Ce₂O₂MnSe₂ were recorded using a JEOL 2100F field emission gun (FEG) transmission electron microscope (TEM) operating at 200 keV. The sample was deposited on a Cu grid and mounted in a double-tilt sample holder. The diffraction patterns were acquired by a Gatan Orius CCD camera.

Powder neutron diffraction (PND). Time-of-flight (TOF) PND data of Ce₂O₂MnSe₂ (~4 g) and (Ce_{0.78}La_{0.22})₂O₂MnSe₂ (~3 g) samples were collected on the General Materials (GEM) Diffractometer at the ISIS facility of the Rutherford Appleton Laboratory (UK). Diffraction data were collected by six detector banks over data ranges of (TOF and d-spacing): PND_bank1 1.1 – 27 ms (1.5 – 36 Å); PND_bank2 1.4 – 20 ms (0.9 – 14 Å); PND_bank3 1.3 – 22 ms (0.45 – 7.7 Å); PND_bank4 1.4 – 20 ms (0.39 – 4.0 Å); PND_bank5 1.5 – 18 ms (0.22 – 2.7 Å); PND_bank6 1.6 – 16 ms (0.18 – 1.8 Å). Each sample was loaded in an 8 mm diameter vanadium can and PND data were acquired at room temperature for 2 h and at 30 K for 2.5 h [Ce₂O₂MnSe₂] or 3.5 h [(Ce_{0.78}La_{0.22})₂O₂MnSe₂]. To follow the magnetic phase transition of (Ce_{0.78}La_{0.22})₂O₂MnSe₂, 5 minute variable temperature PND measurements were recorded on warming from 3 K to 290 K.

Data analysis and refinement. SXRD data of Ce₂O₂MnSe₂ were processed using Bruker APEX2 software and a numerical absorption correction based on the crystal geometry applied. During the integration, a merohedral twinning law [90°, supported by SEM image in Figure S11 of the supporting information (SI)] was applied and satellite peaks up to fourth order were considered. Data were analysed using JANA2006²⁹. The modulated structure model [(3 + 1) D superspace group] was constructed by the Superflip program based on a charge-flipping algorithm.³⁰ Further combined refinements of the structure model were performed using JANA2006 based on the SXRD, PXRD and PND data. Using the supercell approximation, commensurate 3D supercell models were constructed. During the transformation from the (3 + 1)D superspace group to the 3D space group, JANA2006 and Superspace Group Finder³¹ (<http://it.iucr.org/resources/finder/>) were employed to check symmetries of different *t*-sections. TOPAS Academic (TA)³² was employed for the Rietveld refinement of the PXRD and PND data based on supercell models. To refine the **q**-vector of (Ce_{1-x}La_x)₂O₂MnSe₂, TA profile refinement fitted 34 satellite peaks along with the main peaks from average unit cell.

ISODISTORT³³ (<http://stokes.byu.edu/iso/isotropy.php>) was used for the construction of the low temperature magnetic structure. The final magnetic structures were refined using TA from the low temperature PND data. The magnetic ordering of both Mn²⁺ and Ce³⁺ was taken into account. The magnetic form factor of Ce³⁺ appears to be consistently mislabelled as “Ce²⁺” in *International Tables for Crystallography* (Volume C)³⁴ and consequently in the scattering factor databases of TA and other packages. The Ce²⁺ parameters listed in both sources shows excellent agreement with theoretical data³⁵ of Ce³⁺ (see Figure S12). During the TA refinement, a small amount of a MnSe³⁶⁻³⁸ (<1% wt.) impurity phase and weak scattering from the vanadium can were considered. Unless specified otherwise, the diffraction data analysed were recorded at room temperature.

Thermal stability in air. Ce₂O₂MnSe₂ (~0.8 g) was placed in an alumina crucible and heated to different temperatures (from RT to 1200 °C) and held for 1 h at each temperature. The cooled sample was weighed to calculate the mass loss and PXRD patterns were recorded to follow the decomposition.

Magnetic behaviour. Zero-field-cooled (ZFC) and field-cooled (FC) magnetic susceptibility (χ) of ~ 0.1 g Ce₂O₂MnSe₂ and (Ce_{0.78}La_{0.22})₂O₂MnSe₂ samples were measured using a Quantum Design SQUID magnetometer in the temperature range of 2 – 300 K with a 1000 Oe magnetic field. Magnetisation as a function of field was recorded at 5 and 300 K.

Conductivity. The conductivity of a Ce₂O₂MnSe₂ pellet was recorded using a Solatron 1206A impedance analyser from RT to 170 °C. The ac sweeping range was selected as 0.1 – 5 × 10⁶ Hz.

Second-harmonic generation (SHG). Powder SHG measurements were performed on a modified Kurtz-nonlinear optical (NLO) system using a pulsed Nd:YAG laser with a wavelength of 1064 nm. A detailed description of the equipment and methodology has been published³⁹. Unsieved powders were placed in separate capillary tubes and no index matching fluid was used in any of the experiments. The SHG, i.e. 532 nm light, was collected in reflection and detected using a photomultiplier tube. A 532 nm narrow-bandpass interference filter was attached to the tube in order to only detect the SHG light. The SHG measurements were carried out using a ‘single-shot’ at low powder density to avoid sample decomposition. Ce₂O₂MnSe₂ and (Ce_{0.78}La_{0.22})₂O₂MnSe₂ gave comparable SHG signals to quartz, indicating that both are non-centrosymmetric.

RESULT AND DISCUSSION

Synthesis and thermal stability of Ce₂O₂MnSe₂ in air. Using the methods described above high purity (> 99%) bulk samples of Ce₂O₂MnSe₂ and (Ce_{0.78}La_{0.22})₂O₂MnSe₂ could be prepared. The solid solution (Ce_{1-x}La_x)₂O₂MnSe₂ could be prepared for 0 < *x* ≤ 0.7 between 1000 and 1150 °C. For *x* > 0.7, the β -La₂O₂MnSe₂⁴⁰ type phase was formed (Figure S13). In polycrystalline form, Ce₂O₂MnSe₂ appeared black whereas single crystals were orange and translucent. Sample stability was investigated by heating in air. The mass change of Ce₂O₂MnSe₂ heated for 1 hour in air at different temperatures is shown in Figure 2 and PXRD patterns at corresponding

temperatures are shown in Figure S14. $\text{Ce}_2\text{O}_2\text{MnSe}_2$ is stable in air below 250 °C. Between 250 and 400 °C the sample decomposes and there is a mass gain corresponding to the oxidation of Ce^{3+} and Mn^{2+} . At temperatures higher than 400 °C, selenium is lost from the system giving a mass loss and only Ce/Mn oxides are left after heating to temperatures higher than 1100°C. The final oxide mixture of $(\text{Ce}_{1-x}\text{Mn}_x)\text{O}_{2-\delta}$, Mn_3O_4 and Ce_2O_3 formed corresponds to $\sim\text{Ce}_2\text{MnO}_{5.1}$.

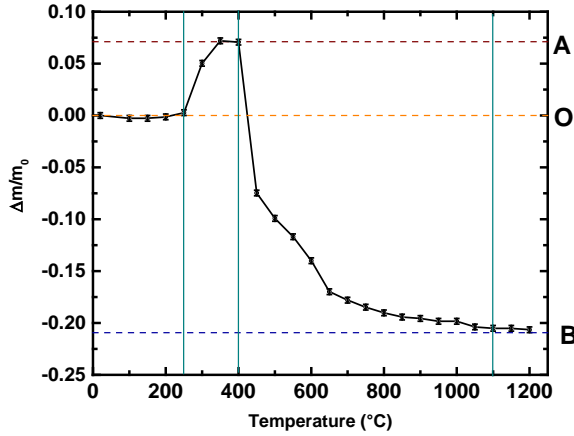


Figure 2. Mass change of $\text{Ce}_2\text{O}_2\text{MnSe}_2$ heated in air at different temperatures. A: oxidation to maximum mass; B: oxide mixture.

Superspace symmetry of $\text{Ce}_2\text{O}_2\text{MnSe}_2$. Electron diffraction patterns of $\text{Ce}_2\text{O}_2\text{MnSe}_2$ down two zone axes are shown in Figure 3. The main diffraction spots can be indexed using the tetragonal parent unit cell (P_4/nmm) reported by Ijjaali *et al.* with cell parameters $a_p = b_p = 4.0260(7)$ Å, $c_p = 9.107(2)$ Å²¹. Indices of diffraction spots based on this parent unit cell are given in the figure. However, weak satellite peaks are observed along $\pm (1\ 1\ 0)$ directions in Figure 3(a) whilst no satellites are observed along $\pm (-1\ 1\ 0)$ directions. This shows that the true symmetry of $\text{Ce}_2\text{O}_2\text{MnSe}_2$ is orthorhombic rather than tetragonal. The component of the modulation vector $\mathbf{q}_p (= \alpha_p \mathbf{a}_p^* + \beta_p \mathbf{b}_p^* + \gamma_p \mathbf{c}_p^*)$ along the $a_p^* + b_p^*$ direction is measured to be $\alpha_p = \beta_p \approx \pm 0.079$. In this paper $\mathbf{q} (= \alpha \mathbf{a}^* + \beta \mathbf{b}^* + \gamma \mathbf{c}^*)$ is shortened to $(\alpha\ \beta\ \gamma)$ and the subscript p refers to the parent unit cell. From SXRD data, the modulation vector \mathbf{q}_p was confirmed to be $(0.079\ 0.079\ 0.5)$. From the parent space group and modulation vector $\mathbf{q}_p = (\alpha_p\ \alpha_p\ \frac{1}{2})$, the $(3+1)$ D superspace group was obtained using ISODISTORT^{33,41}. To coincide with the modulated symmetry, an orthorhombic unit cell was defined as $\sim \sqrt{2}a_p \times \sqrt{2}b_p \times c_p$. The modulation vector $\mathbf{q} (= \alpha \mathbf{a}^* + \beta \mathbf{b}^* + \gamma \mathbf{c}^*)$ based on this orthorhombic unit cell is $(0.16\ 0\ 0.5)$. Non-standard settings of the superspace group were used to aid comparison with published work on $\text{Ln}_2\text{O}_2\text{MSe}_2$ materials (with layers stacked along c axes). There are four different irreducible representation possibilities: $S_1\ Cmme(\alpha_0\frac{1}{2})$ [67.11], $S_2\ Cmme(\alpha_0\frac{1}{2})oso$ [67.12], $S_3\ Cmme(\alpha_0\frac{1}{2})$ [67.11] and $S_4\ Cmme(\alpha_0\frac{1}{2})oso$ [67.12] (space group symbol is $Cmma$ in the old version international tables), which are non-standard settings of $Acmm(\frac{1}{2}oy)$ [67.11] and $Acmm(\frac{1}{2}oy)oso$ [67.12]. The satellite reflection condition

of $Cmme(\alpha_0\frac{1}{2})$ [67.11] is $HKom: H = 2n$, whilst those of $Cmme(\alpha_0\frac{1}{2})oso$ [67.12] are $HKom: H = 2n$ and $HoLm: m=2n$.⁴² Thus, the difference between these two superspace groups is in the $(HoLm)$ reflections. The $(hk\frac{1}{2})$ or $(HKlm)$ section of reciprocal space, which contains only satellite reflections, is reconstructed from the SXRD data in Fig 3c (note that $L = 2l$ where l is the reflection index based on the parent cell.). In this figure, strong first order satellite reflections ($m = 1$) are observed, but $(H011)$ and $(H01\bar{1})$ reflections are absent. Thus, systematic absences indicate that $Cmme(\alpha_0\frac{1}{2})oso$ [67.12] group is the appropriate choice. Because of the modulation, the centrosymmetric nature of the average 3D space group $Cmme$ is lost, which is consistent with the weak SHG effect observed.

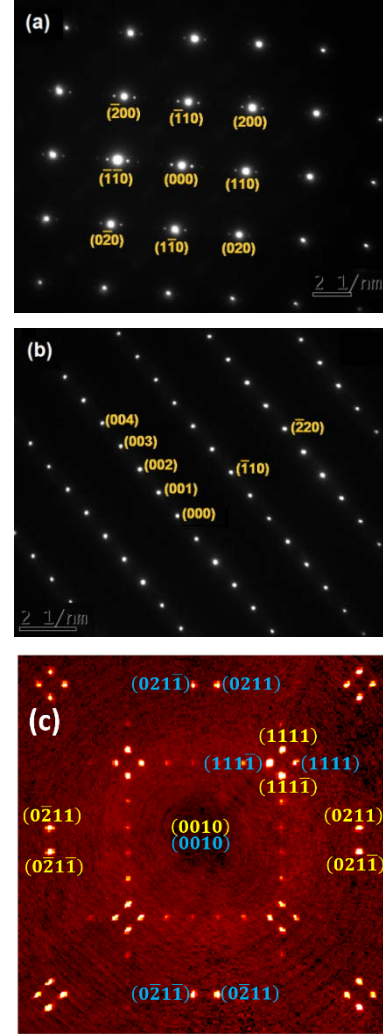


Figure 3. (a) $[0\ 0\ 1]$ and (b) $[1\ 1\ 0]$ zone axis electron diffraction patterns of $\text{Ce}_2\text{O}_2\text{MnSe}_2$. The indices of main reflections are based on the tetragonal parent unit cell $a_p = b_p = 4.0260(7)$ Å, $c_p = 9.107(2)$ Å.²¹ Satellite reflections are observed along $\pm [1\ 1\ 0]$ directions. (c) $(HKlm)$ cross section of merged SXRD patterns indexed using the $\sqrt{2}a_p \times \sqrt{2}b_p \times c_p$ unit cell. Indices with different colors are from the two twin domains. $(H011)$ and $(H01\bar{1})$ reflections are absent. For example, $(-2\ 0\ 1\ -1)$ and $(-2\ 0\ 1\ 1)$ reflections from the cyan domain would lead to a “diamond” pattern of reflections

close to the (0 -2 1 1) and (0 -2 1 -1) reflections of the yellow domain if present.

Structure of $Ce_2O_2MnSe_2$. The structure of $Ce_2O_2MnSe_2$ was solved from single crystal data using Superflip with no symmetry specified and the space group $Cmme(\alpha_0\frac{1}{2})oso$ [67.12] with $a = 5.681(2)$ Å, $b = 5.679(2)$ Å, $c = 9.096(2)$ Å was confirmed. The superspace group and structure obtained correspond to the S_4 irrep proposed from ISODISTORT analysis. The Fourier maps of Figure 4 show that the Mn site occupancy is strongly modulated. Beginning with the Superflip model, combined refinements using the SXRD, PXRD, and PND (d-spacing range 0.39 – 12 Å) data were performed. During refinement, four position modulation waves were employed for Ce, Se, and O. One crenel occupancy modulation wave (length = 0.5, centre at 0.75) and four Legendre polynomial terms in crenel interval were used to describe positional modulations of Mn. Isotropic atomic displacement parameters (ADPs) were applied to all the atoms. There was no significant improvement in fit by adding more modulation wave terms or using ADP modulation. The refined model is summarised in Table 1, Table 2 and Table S1. The refinements give good agreement with the diffraction data and the modulation vector refined to $\mathbf{q} = [0.158(1) \ 0 \ 0.5]$ from PXRD. The refined \mathbf{q} is slightly different to that from SXRD of $[0.164(1) \ 0 \ 0.5]$, which may be caused by a slight composition difference between the powder and single crystal samples. Work on related systems shows that partial oxidation of Ce^{3+} to Ce^{4+} can occur on reheating powdered samples and can influence \mathbf{q} ²⁸.

The average structure model, occupancy modulation wave of Mn and displacement modulation waves of all atoms are shown in Figure 5. The positions of Ce, Se and O are mainly modulated along the x_2 direction and the position of Mn mainly along the x_1 direction, where x_i ($i = 1 - 4$) are the superspace axes⁴³. The Mn x_1 displacement is intimately related to the local site ordering and discussed in more detail below. Along the x_2 (b) direction, Se displacements above and below the Mn plane in the same $[MnSe_{4/2}]^{2-}$ layer are out-of-phase whilst all O and Ce displacements in the same $[Ce_2O_2]^{2+}$ layer are in-phase. Neighbouring/bonded Se and Ce atoms are also modulated in-phase, so that the modulation involves relatively rigid $OCe_{4/4}$ tetrahedra with the major local coordination distortions occurring within the $MnSe_{4/2}$ tetrahedral layers.

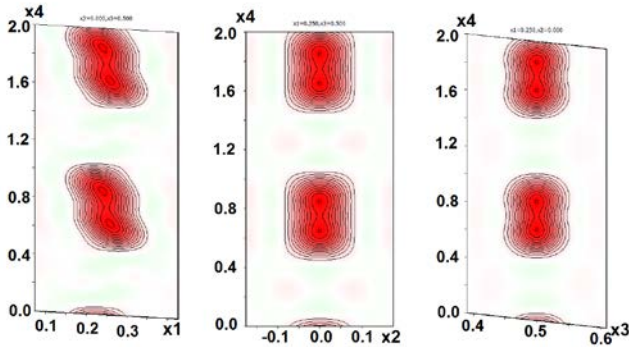


Figure 4. Fourier electron density maps of $Ce_2O_2MnSe_2$ centred at Mn (0.25 0 0.5) from charge flipping. (x_1 - x_4 , x_2 - x_4 , x_3 - x_4 cross sections).

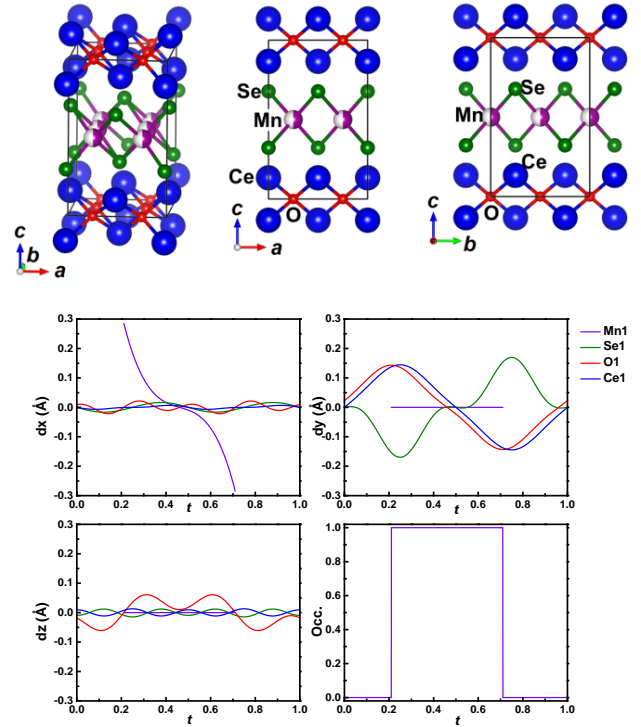


Figure 5. Average structure, displacement and occupancy modulation wave of $Ce_2O_2MnSe_2$. The atoms labelled are the reference atoms in the modulation wave plot. Mn sites are shown as half spheres to reflect their average site occupancy.

Table 1. Refined cell parameters of $Ce_2O_2MnSe_2$ from PXRD data.

Symmetry	Orthorhombic
Superspace group	$Cmme(\alpha_0\frac{1}{2})oso$ [67.12]
a (Å)	5.6798(3)
b (Å)	5.6777(3)
c (Å)	9.1055(1)
V (Å ³)	293.7(1)
α	0.158(1) ^(a)
d_{theory} (g/cm ³)	5.94(1)
Z	2

^(a): Refined from PXRD data. SXRD gave 0.164(1).

Table 2. Refined atomic coordinates and modulation waves of Ce₂O₂MnSe₂.

Atomic coordinates						
	Site	x	y	z	U _{iso} (Å ²)	Occupancy
Ce	4g	0	0.25	0.13346(5)	0.00411(12)	1
Se	4g	0	0.25	0.67756(5)	0.00656(12)	1
Mn	4b	0.25	0	0.5	0.0080(3)	1 ^a
O	4a	0.25	0	0	0.00114(18)	1
Displacement modulation waves						
	Type	Order	x	y	z	
Ce	sin	1	0	0.02149(10)	0	
	cos	1	0	-0.00959(5)	0	
	sin	2	-0.00062(12)	0	-0.00014(11)	
	cos	2	0.00070(13)	0	-0.00013(10)	
	sin	3	0	-0.00059(5)	0	
	cos	3	0	0.00183(15)	0	
	sin	4	0.00005(3)	0	0.0012(2)	
	cos	4	0.0004(3)	0	-0.00013(2)	
Se	sin	1	0	0.01140(9)	0	
	cos	1	0	0.01834(15)	0	
	sin	2	0.00128(15)	0	-0.0003(2)	
	cos	2	-0.0026(3)	0	-0.00013(11)	
	sin	3	0	0.0082(3)	0	
	cos	3	0	-0.00081(3)	0	
	sin	4	0.0000(3)	0	-0.0010(3)	
	cos	4	0.0000(3)	0	0.0008(2)	
O	sin	1	0	0.0229(4)	0	
	cos	1	0	0	-0.0050(3)	
	sin	2	-0.0014(12)	0	0	
	cos	2	0	0	0	
	sin	3	0	-0.0023(13)	0	
	cos	3	0	0	0.0039(5)	
	sin	4	0.0028(16)	0	0	
	cos	4	0	0	0	
Mn	Legendre	1	-0.0341(6)	0	0	
	Legendre	2	0	0	0	
	Legendre	3	-0.0162(14)	0	0	
	Legendre	4	0	0	0	

Crenel occupancy modulation wave

Mn	Width	0.5	Centre at	0.75
----	-------	-----	-----------	------

^(a): Taking the occupancy wave into consideration, the average occupancy of Mn is 0.5.

Modulated Mn-Se and O-Ce bond lengths are shown in Figure SI5 and selected Ce-O-Ce and Se-Mn-Se bond angles are plotted in Figure 6. Ce-O bond lengths vary from 2.32(1) – 2.38(1) Å with an average value of 2.35(1) Å and Mn-Se from 2.52(1) – 2.65(1) Å with an average value 2.57(1) Å. The Ce-O-Ce bond angles vary from 104.8(5) – 120.9(2)° and Se-Mn-Se from 100.9(1) – 126.1(1)°. As a comparison, bond lengths and angles of Ce-O and Ce-O-Ce in layered $\text{Ce}_4\text{O}_4\text{Se}_3$ ⁴⁴ are 2.312(5) – 2.412(4) Å and 101.3(1) – 137.3(5)°. In zinc-blende MnSe systems⁴⁵ (ICSD #24252), the bond length of Mn-Se is 2.52 Å and in layered TlCuMnSe_2 ⁴⁶, Mn-Se bond length and angles are 2.52 Å and 107.6 – 110.4°. The coordination environments in modulated $\text{Ce}_2\text{O}_2\text{MnSe}_2$ model are therefore in good agreement with those expected from related systems. The bond valence sums of Ce^{3+} , Mn^{2+} , Se^{2-} and O^{2-} calculated using the reference parameters in the JANA database vary from 2.77 – 2.93, 1.95 – 2.11, 1.75 – 1.94, and 1.98 – 2.01, respectively, giving further confidence in the chemical plausibility of our model.

Because the sum of the ionic radii of Mn^{2+} and Se^{2-} is larger than that of Ce^{3+} and O^{2-} in $\text{Ce}_2\text{O}_2\text{MnSe}_2$,⁴⁷ there is an inherent size mismatch between undistorted $[\text{Ce}_2\text{O}_2]^{2+}$ and $[\text{MnSe}_4]^{2-}$ layers. For ideal OCe_4 and MnSe_4 tetrahedra the

mismatch is around 7% (a 2D slab of $\text{OCe}_{4/4}$ would have $a_p = 3.931$ Å and $\text{MnSe}_{4/2}$ 4.069 Å). However, the ionic interaction between the positively and negatively charged slabs requires a composition match which will impose a strain on one or both layers. This strain gives rise to both distortions in the average structure and to the modulations observed. In terms of the average structure the compression of MnSe_4 tetrahedra in the ab plane gives rise to (Figure 6a) $\text{Se}_1(1)\text{-Mn}_1(1)\text{-Se}_1(4)'$ and $\text{Se}_1(2)\text{-Mn}_1(1)\text{-Se}_1(3)'$ angles less than 109.5° and others larger than 109.5°. For the MnSe_4 tetrahedra, $\text{Se}_1(1)\text{-Mn}_1(1)\text{-Se}_1(4)'/\text{Se}_1(2)\text{-Mn}_1(1)\text{-Se}_1(3)'$ bond angles average around 102° and $\text{Se}_1(1)\text{-Mn}_1(1)\text{-Se}_1(2)/\text{Se}_1(3)\text{-Mn}_1(1)\text{-Se}_1(4)'$ bond angles around 113°. Because of the considerable displacement modulation of Mn along the x_2 direction, the bond angle of $\text{Se}_1(2)\text{-Mn}_1(1)\text{-Se}_1(4)'$ and $\text{Se}_1(1)\text{-Mn}_1(1)\text{-Se}_1(3)'$ are strongly modulated. Since OCe_4 tetrahedra are under tension in the ab plane, the average $\text{Ce}_1(2)\text{-O}_1(1)\text{-Ce}_1(3)'$ and $\text{Ce}_1(1)\text{-O}_1(1)\text{-Ce}_1(4)'$ bond angles are larger than 109.5° and the others smaller than 109.5°. The higher rigidity of the $[\text{Ce}_2\text{O}_2]^{2+}$ layers are reflected in a smaller tetrahedral bond angle modulation.

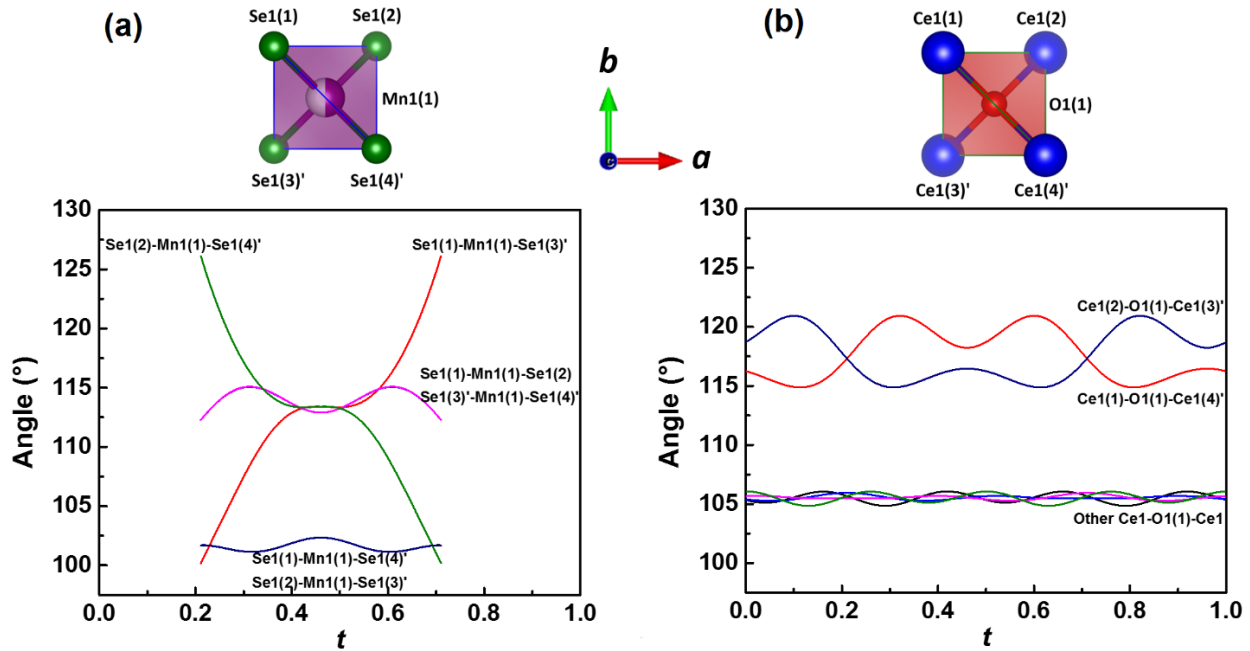


Figure 6. Se-Mn-Se (a) and Ce-O-Ce (b) bond angles in $\text{Ce}_2\text{O}_2\text{MnSe}_2$. In (a), $\text{Se}_1(1)$, and $\text{Se}_1(4)'$ are above the Mn plane and $\text{Se}_1(2)$ and $\text{Se}_1(3)'$ are below the Mn plane; in (b) $\text{Ce}_1(1)$, and $\text{Ce}_1(4)'$ are above the O plane and $\text{Ce}_1(2)$, and $\text{Ce}_1(3)'$ are below the O plane.

To help visualise how Mn occupancy modulations further relieve the strain in one dimension, the modulated structure can be approximated using the commensurate vector $\mathbf{q} = (3/19 \ 0 \ 1/2)$ allowing an approximate supercell structure ($19a \times b \times 2c$). Transforming from the $(3 + 1)\text{D}$ superspace group to the 3D space group, there are two high symmetry space groups along different t -sections: $Imcb$ (72) when $t = 1/76 +$

$n/38$ and $Ibca$ (73) when $t = n/38$ ($n = \text{integer}$) and one low symmetry space group along general t -sections: $I2cb$ (45).^{29,31} Starting with these supercells, further refinements against the PXRD and PND data were conducted using TA to check the reliability of our models. All supercell models give an excellent fit to the diffraction data with deviation of atomic coordinates of $< \pm 0.1$ Å. Typical fitted profiles based on the

Imcb model are shown in Figure 7. All the profiles are shown in Figures SI6 & 7. Structure parameters for each model (*Imcb*, *Ibca* and *Izcb*) are given as SI CIF files.

The view along the *b* axes and Mn ordering patterns within the $[\text{MnSe}_{4/2}]$ layers of the two higher symmetry models are shown in Figure 8; the Mn occupancy of alternating $[\text{MnSe}_2]$ layers is out of phase. If we consider the *Imcb* model, we can see that it contains blocks of 5 or 6 corner-sharing tetrahedra (as found in $\text{La}_2\text{O}_2\text{CdSe}_2$) separated by a pair of edge-sharing tetrahedra (as found in layered $\text{Ce}_2\text{O}_2\text{FeSe}_2$). After submission of this work, a similar ordering pattern was reported for a closely related composition using a lower symmetry modulated structural model.[ref] Whilst the Mn-Mn distance is significantly smaller in edge-shared tetrahedra than corner-shared (~ 3.2 vs ~ 4 Å), the separation of Mn rows along the *a* axis for edge-shared tetrahedra is significantly larger than for corner-shared (here 3.23 vs 2.77 Å on average). The resultant local distortions are the origin of the significant modulation of Mn coordinate along x_1 . By mixing corner- and edge-sharing connections in this way, the $[\text{MnSe}_{4/2}]^{2-}$ layers size-match the $[\text{Ce}_2\text{O}_2]^{2+}$ layers, in which the neighbouring O-O (centre of OCe_4 tetrahedra) distance along the *a* axis is ~ 2.84 Å on average.

The difference between the different possible supercell models is the Mn occupancy in the row of $\text{MnSe}_{4/2}$ edge-shared tetrahedra at the *a* value indicated by the arrows in Figure 8. In the *Ibca* model, all these tetrahedra are 50% occupied by Mn (the Mn are at the edge of crenel occupancy steps). In the *Imcb* model, they are either occupied or empty (ordered arrangement). The final *Izcb* model has the same Mn ordering pattern as the *Imcb* model but the mirror symmetry perpendicular to the *a* axis is removed. The three different models come from the different choices of the $x_4(t)$ values. If the system is an ideal commensurate one and can be described by the smallest $n_1a \times n_2b \times n_3c$ supercell ($n_1, n_2, n_3 = \text{integers}$), the possible $x_4(t)$ choices are an $n_1 \times n_2 \times n_3$ discrete series, i.e. $n/(n_1 \times n_2 \times n_3) + t_0$ ($n = \text{integers}$ and t_0 is the “origin”)⁴³. Thus, if an $\text{Ln}_2\text{O}_2\text{MnSe}_2$ material were an ideal commensurate system, it would adopt only one of these three commensurate models with $t = n/38 + t_0$ according to the choice of t_0 . The calculated PXRD patterns of the three

possible models are shown in Figure SI8. There are only very small intensity differences (around 0.1%) between them, which makes distinguishing between the different possibilities hard.

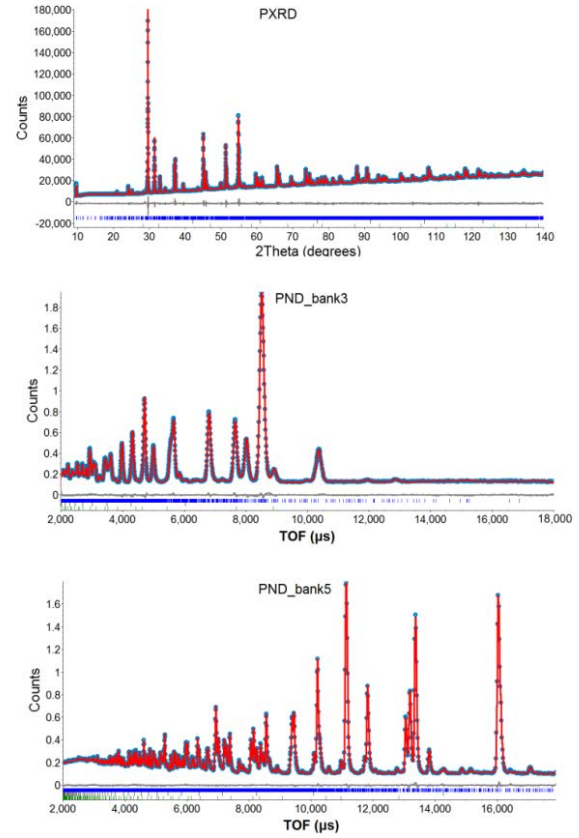


Figure 7. Typical Rietveld refinement profiles of $\text{Ce}_2\text{O}_2\text{MnSe}_2$ from combined refinement using *Imcb* supercell model. Dots: observed; solid line: calculated curve; grey line below: difference curve; vertical tick marks: peak positions.

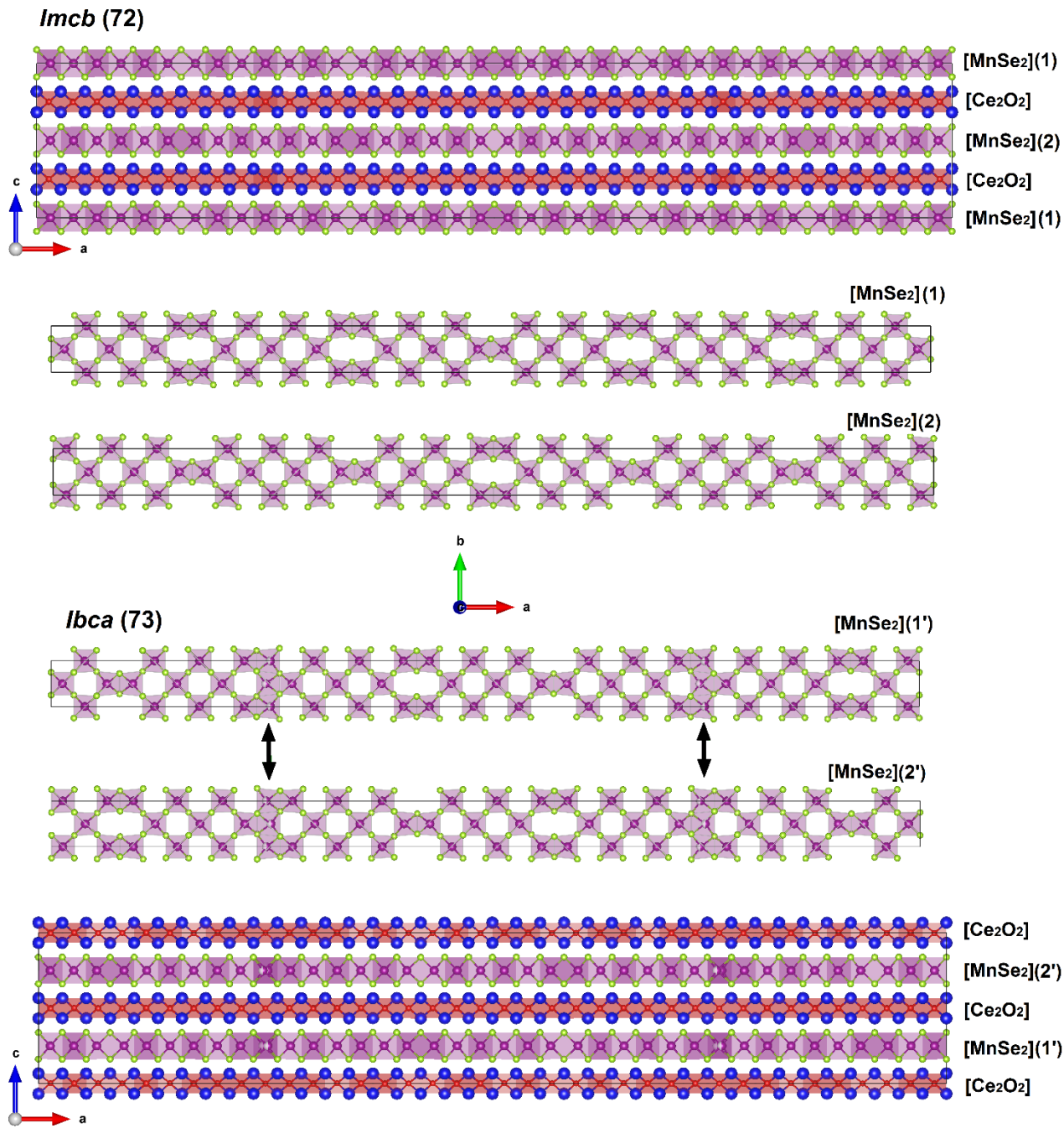


Figure 8. Mn ordering patterns in $[\text{MnSe}_2]$ layer of different commensurate approximate models. Layers are projected along c axes and there are two layers (shifted $b/2$) in each unit cell. $\text{MnSe}_{4/2}$ tetrahedra are illustrated. The tetrahedra marked by arrows in $Ibca$ are half occupied by Mn. The Mn occupancy of alternating $[\text{MnSe}_{4/2}]$ layers is out of phase

Structure of $(\text{Ce}_{0.78}\text{La}_{0.22})_2\text{O}_2\text{MnSe}_2$. Because the occupancy modulation of Mn in $\text{Ce}_2\text{O}_2\text{MnSe}_2$ arises from the size mismatch between oxide and chalcogenide layers, the modulation vector can be controlled by partially substituting Ce^{3+} by larger La^{3+} . $(\text{Ce}_{1-x}\text{La}_x)_2\text{O}_2\text{MnSe}_2$ solid solutions can be formed for $x = 0 - 0.7$. The modulation vector component α and cell volume across the series are plotted in Figure 9. Within error, $(\text{Ce}_{0.78}\text{La}_{0.22})_2\text{O}_2\text{MnSe}_2$ can be considered as a simple commensurate case, in which the $(3 + 1)$ D superspace group is $Cmme(\alpha_0^{\frac{1}{6}})oso$ [67.12] with $\alpha = 1/6$. The $(3 + 1)$ D superspace model of $\text{Ce}_{0.78}\text{La}_{0.22})_2\text{O}_2\text{MnSe}_2$ refined using the

PXRD and PND data is given as a SI cif file. When trying to choose a commensurate 3D description, there are again three possible structure models at different t -sections: $B2eb$ (41, old symbol $B2cb$) when t is general value, $Bbeb$ (68, old symbol $Bbcb$) when $t = 1/24 + n/6$ or $t = 1/8 + n/6$, and $Bmcb$ (64, old symbol $Bmab$) when $t = n/6$ or $t = 1/12 + n/6$ with $n = \text{integer}$.²⁹ The supercell models were constructed using JANA2006 from the $\text{Ce}_2\text{O}_2\text{MnSe}_2$ incommensurate model and further Rietveld refinements were conducted in TA using the PXRD and PND data. The Mn ordering patterns are similar to those shown in Figure 8 for $\text{Ce}_2\text{O}_2\text{MnSe}_2$ but with blocks

of 5 corner-sharing tetrahedra separating each edge-shared pair. The fitted profiles are shown in Figures SI9-11 in the supporting information (SI). The structural parameters for the two higher symmetry models (*Bmcb* and *Bbeb*) are listed in Table SI2 and Table SI3. Details of the *B2eb* model (which has a similar Mn ordering pattern to the *Bmcb* model but has no mirror perpendicular to the *a* axis) are given in Table 3. The calculated PXRD patterns of the three possible models are compared in Figure SI12. There is very small intensity

difference ($< 0.3\%$) between them. The positive SHG measurement suggests the *B2eb* model for $\text{Ce}_{0.78}\text{La}_{0.22}\text{O}_2\text{MnSe}_2$; however, the noncentrosymmetric *B2eb* and centrosymmetric *Bmcb* model give essentially indistinguishable fits to the current diffraction data. We therefore use the simpler *Bmcb* model for structural discussions.

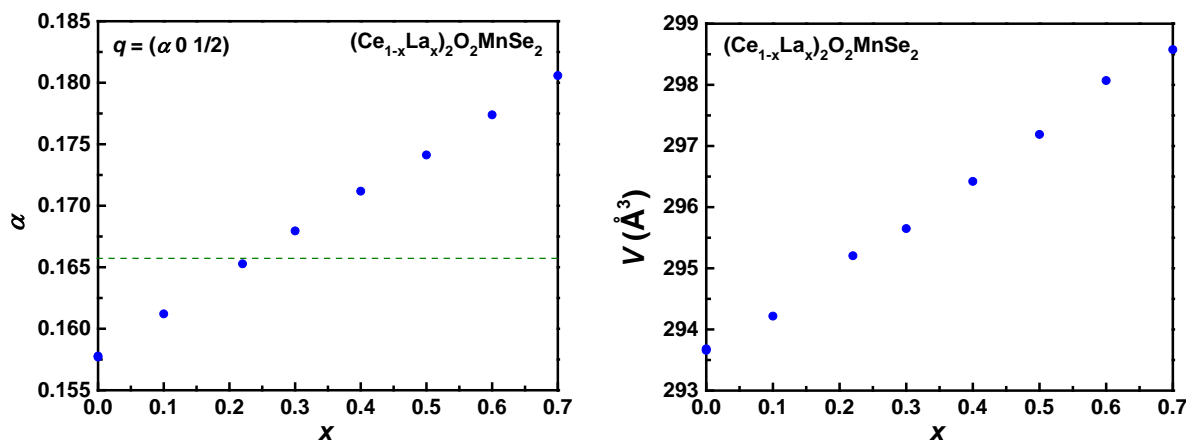


Figure 9. Modulation vector and cell volume of $(\text{Ce}_{1-x}\text{La}_x)_2\text{O}_2\text{MnSe}_2$ solid solution. The horizontal dashed line indicates the ideal $\alpha = 1/6$. Errors in α are estimated to be ± 0.001 by profile fitting.

Table 3. Structure parameters of (Ce_{0.78}La_{0.22})₂O₂MnSe₂ by supercell description (Model 3) ^(a).

<i>t</i>	general					
Space Group	B2eb (41)					
a (Å)	34.1489(1)					
b (Å)	5.68892(4)					
c (Å)	18.22496(3)					
V (Å ³)	3540.57(3)					
d _{theory} (g/cm ³)	5.904(1)					
R _{wp} (%)	2.57 (overall), 2.52 (PXR), 7.85 (PND_bank1), 5.78 (PND_bank2), 3.19 (PND_bank3), 2.75 (PND_bank4), 2.34 (PND_bank5), 2.80 (PND_bank6).					
	Site	x	y	z	Occupancy	B _{eq} (Å ²)
Ce1/La1	8b	0.9161(9)	0.7253(9)	0.3159(6)	0.78/0.22	0.45(3)
Ce2/La2	8b	0.7503(8)	0.7337(18)	0.3139(5)	0.78/0.22	0.45(3)
Ce3/La3	8b	0.5835(9)	0.763(2)	0.3181(7)	0.78/0.22	0.45(3)
Ce4/La4	8b	0	0.2271(14)	0.3183(5)	0.78/0.22	0.45(3)
Ce5/La5	8b	0.8329(4)	0.2413(12)	0.3196(7)	0.78/0.22	0.45(3)
Ce6/La6	8b	0.6669(5)	0.245(2)	0.3159(6)	0.78/0.22	0.45(3)
Se1	8b	-0.0014(9)	0.7400(19)	0.4132(8)	1	0.76(4)
Se2	8b	0.8309(6)	0.729(2)	0.4102(9)	1	0.76(4)
Se3	8b	0.6665(7)	0.749(3)	0.4127(9)	1	0.76(4)
Se4	8b	0.0814(7)	0.230(3)	0.4097(9)	1	0.76(4)
Se5	8b	0.9153(8)	0.2268(16)	0.4103(8)	1	0.76(4)
Se6	8b	0.7488(9)	0.246(3)	0.4137(9)	1	0.76(4)
O1	8b	0.8735(11)	-0.027(5)	0.2503(10)	1	0.40(4)
O2	8b	0.7067(10)	-0.007(7)	0.2492(13)	1	0.40(4)
O3	8b	0.5399(8)	0.020(7)	0.2541(11)	1	0.40(4)
O4	8b	0.7904(9)	0.489(5)	0.2464(11)	1	0.40(4)
O5	8b	0.6241(10)	0.501(7)	0.2544(12)	1	0.40(4)
O6	8b	0.4568(9)	0.528(5)	0.2542(11)	1	0.40(4)
Mn1	4a	0.3694(10)	0	0	1	0.77(5)
Mn2	4a	0.2082(10)	0	0	1	0.77(5)
Mn3	4a	0.0383(8)	0	0	1	0.77(5)
Mn4	4a	0.7879(9)	0	0	1	0.77(5)
Mn5	4a	0.6234(10)	0	0	1	0.77(5)
Mn6	4a	0.4624(10)	0	0	1	0.77(5)

^(a): The x coordinate of Ce4/La4 was fixed to 0 to avoid origin shift during refinement.

Structural relationships between Ce₂O₂MnSe₂/(Ce_{0.78}La_{0.22})₂O₂MnSe₂ and other layered Ln₂O₂MSe₂. The layered Ln₂O₂MSe₂ materials (Ln = La, Ce; M = Fe, Mn, Zn, Cd) reported up to now have similar structures based on alternate stacking of [Ln₂O₂]²⁺ and [MSe_{4/2}]²⁻ layers. The difference between them is the ordering patterns within [MSe_{4/2}] layers and thus the symmetry of the system. The analysis above reveals that each of the cation-ordered structures can be described using the same **q_p** vector ($\alpha_p \alpha_p 1/2$)³³ (in reciprocal space) relative to the parent

structures and they can therefore all be derived from a single superspace structural model in *Cmme*($\alpha_0 \frac{1}{2}$)*oso* [67.12] with **q** = $\alpha \mathbf{a}^* + \alpha \mathbf{b}^* + 0.5 \mathbf{c}^*$. Using this **q** vector classification, the relation of [MSe_{4/2}] ordering patterns in different Ln₂O₂MSe₂ materials can be summarised as in Figure 10. The value of α ($\alpha = 2 \alpha_p$) varies from 0 in La₂O₂CdSe₂ to 1 in Ce₂O₂FeSe₂ (La₂O₂FeSe₂). The symmetry of each is the corresponding symmetry at the ($\alpha_p \alpha_p 1/2$) point in reciprocal space of the parent structure. The disordered Ln₂O₂MSe₂ parent structure

has D_{4h} symmetry with the space group $P4/nmm$ (129)²¹. In $\text{La}_2\text{O}_2\text{CdSe}_2$ ²³, the \mathbf{q}_p vector is Z (0 0 1/2) [IR Z_4^- using ISODISTORT nomenclature] giving D_{4h} symmetry and space group $P4_2/nmc$ (137). In $\text{Ce}_2\text{O}_2\text{FeSe}_2$ ²⁵ and $\text{La}_2\text{O}_2\text{FeSe}_2$ ²⁶, the \mathbf{q}_p vector is A (1/2 1/2 1/2) [IR A_2] giving D_{2h} symmetry and space group $Imcb$ (72). In $\text{La}_2\text{O}_2\text{ZnSe}_2$ ²⁷, $\text{Ce}_2\text{O}_2\text{ZnSe}_2$, $\text{Ce}_2\text{O}_2\text{MnSe}_2$ and $(\text{Ce}_{0.78}\text{La}_{0.22})_2\text{O}_2\text{MnSe}_2$ the \mathbf{q}_p vector is S (α_p 1/2) [$\alpha' \neq 0$ or 1/2, IR S_4] with D_{2h} symmetry. In each case there would be three similar supercell models to describe each. Here we only discuss the completely site ordered model $Imcb$ (72) when $\alpha = 2n+1/2n'+1$ or $Bmcb$ (64) when $\alpha = 2n+1/2n'$ (n, n' are integers)^{29,31} as all the reported systems show this ordering type.

If we define the connection type of $\text{MSe}_{4/2}$ tetrahedra in $\text{La}_2\text{O}_2\text{CdSe}_2$ as “C” (corner-sharing, checkboard-like) and the connection type of $\text{MSe}_{4/2}$ tetrahedra in $\text{Ce}_2\text{O}_2\text{FeSe}_2$ as “E” (edge-sharing, stripe-like), we can adopt a straightforward real space description of the different ordering patterns in terms of different C:E ratios. C:E is 1:0 in $\text{La}_2\text{O}_2\text{CdSe}_2$, 3:1 (3C-1E) in $\text{La}_2\text{O}_2\text{ZnSe}_2$, 4:1 (4C-1E) in $\text{Ce}_2\text{O}_2\text{ZnSe}_2$, 5:1 (5C-1E) in $(\text{Ce}_{0.78}\text{La}_{0.22})_2\text{O}_2\text{MnSe}_2$, 16:3 or $5^{1/3}:1$ (5C-1E-6C-1E-5C-1E) in $\text{Ce}_2\text{O}_2\text{MnSe}_2$ and 0:1 in $\text{Ce}_2\text{O}_2\text{FeSe}_2$ ($\text{La}_2\text{O}_2\text{FeSe}_2$). Figure 10 shows that the ratio of C:E can be expressed as $(1-\alpha)/\alpha$ such that the $(\text{Ce}_{1-x}\text{La}_x)_2\text{O}_2\text{MnSe}_2$ solid solution samples of Figure 9 range from a C:E of $5^{1/3}:1$ to $\sim 4.5:1$.

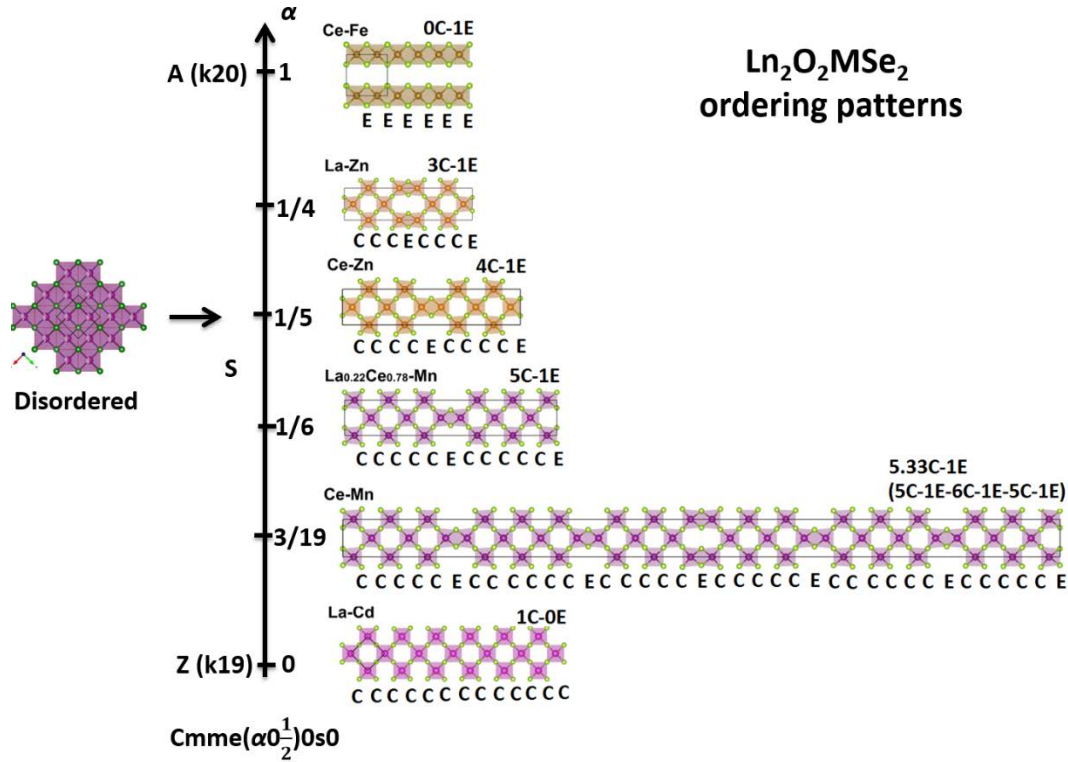


Figure 10. Relationship of different $[\text{MSe}_{4/2}]^{2-}$ ordering patterns in $\text{Ln}_2\text{O}_2\text{MSe}_2$. Structures are labelled by Ln-M. The connection type of $\text{MSe}_{4/2}$ tetrahedra in $\text{La}_2\text{O}_2\text{CdSe}_2$ is defined as “C” (corner-sharing, checkboard-like) and the connection type of $\text{MSe}_{4/2}$ tetrahedra in $\text{Ce}_2\text{O}_2\text{FeSe}_2$ is defined as “E” (edge-sharing, stripe-like). The other structures have C and E connections in different ratios.

This overview of the structures in terms of C and E connections helps rationalise the incommensurate/modulated nature of $\text{Ce}_2\text{O}_2\text{MnSe}_2$. For a given $[\text{A}_2\text{O}_2]^{2+}$ and $[\text{MSe}_{4/2}]^{2-}$ combination there will be an inherent size mismatch of layers which can be partially compensated by local tetrahedral distortions as discussed above. The 50% occupied systems have a second strain-relieving mechanism available in that C units are inherently smaller than E units. For a given MSe_2 layer the ratio of C:E will therefore increase as the $[\text{Ln}_2\text{O}_2]^{2+}$ layer is made smaller. For example, in the (Ce,La)-Mn system the larger $[(\text{La}_{0.22}\text{Ce}_{0.78})_2\text{O}_2]^{2+}$ layer has a commensurate 5C-1E structure and decreasing the $[\text{A}_2\text{O}_2]^{2+}$ size switches to the more C-rich $\sim 5^{1/3}\text{C-1E}$ structure of the pure Ce phase. This also rationalises the modulated satellite reflections reported recently for $\text{Ce}_{2-x}\text{O}_2\text{ZnSe}_2$ systems.²⁸

Low temperature magnetic structure of $(\text{Ce}_{0.78}\text{La}_{0.22})_2\text{O}_2\text{MnSe}_2$. Powder neutron diffraction (bank3) data of $(\text{Ce}_{0.78}\text{La}_{0.22})_2\text{O}_2\text{MnSe}_2$ recorded at different temperatures are plotted in Figure 11(a) [data from other banks are shown in Figure S13]. Several magnetic diffraction peaks (labelled as $m_1 - m_5$) appear below 150K. The intensities of these magnetic peaks at different temperatures are plotted in Figure 11(b) and (c). With decreasing temperature, peaks m_1, m_2 and m_3 increase in intensity and reach a maximum at $\sim 40\text{K}$ whereas m_4 and m_5 increase monotonically. This suggests that two magnetic ordering processes occur (ordering of Mn^{2+} and ordering of Ce^{3+}). Similar behaviour has been observed in related systems^{25,48}.

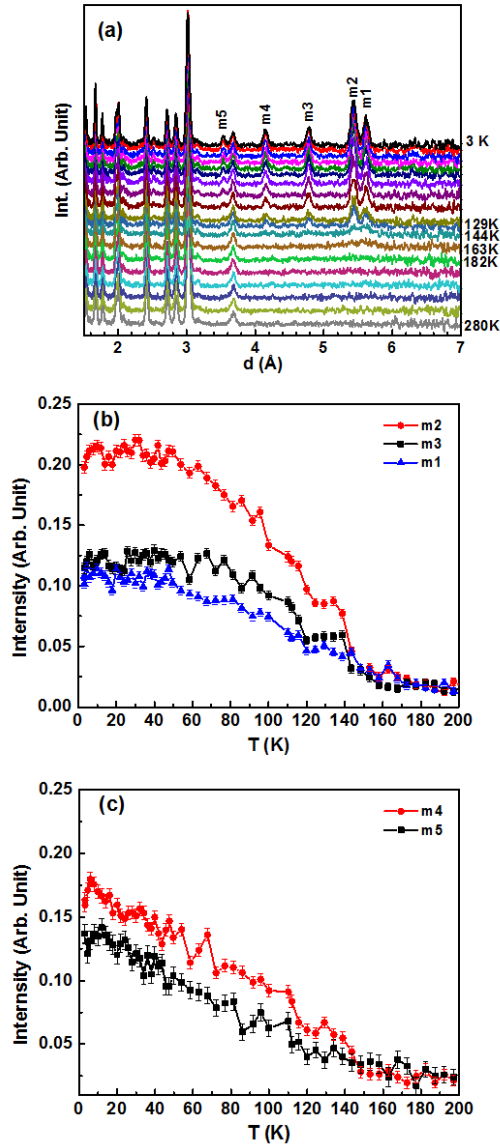


Figure 11. PND (bank 3) data (a) and intensity of magnetic peaks (b) (c) of $(\text{Ce}_{0.78}\text{La}_{0.22})_2\text{O}_2\text{MnSe}_2$ at different temperatures. Selected magnetic peaks are labelled m_1 to m_5 .

Pawley refinement was used to confirm that all magnetic peaks could be indexed with the nuclear unit cell. Using ISODISTORT magnetic structures at k points consistent with this observation were generated and a good fit was obtained using an mY_2 - model, containing an antiferromagnetic arrangement of Mn^{2+} moments. Magnetic refinements were performed in Shubnikov group P_21nma (62.455), which allows 15 magnetic degrees of freedom (moment directions and amplitudes on Mn^{2+} and Ce^{3+}) and gave an excellent fit to the experimental data. We could obtain an equivalent fit with magnetic moments of each Mn^{2+} or Ce^{3+} constrained to have the same magnitude, with the spin direction of Mn^{2+} constrained to lie parallel to the c axes of nuclear model and with that of Ce^{3+} within the ab plane of nuclear model as shown in Figure 13. An excellent fit was thus obtained with only two degrees of freedom. Due to their small magnitude

the directions of Ce moments are less well determined than Mn, but R_{wp} agreement factors showed a clear minimum at the orientations reported. Atomic coordinates showed only small deviation ($\pm 0.1 \text{ \AA}$) from the RT nuclear structure. The Rietveld profile of 30K PND_bank3 data of $(\text{Ce}_{0.78}\text{La}_{0.22})_2\text{O}_2\text{MnSe}_2$ is shown in Figure 12(a) and the profiles of PND bank1 – bank5 are shown in Figure S14.

The magnetic structure of $(\text{Ce}_{0.78}\text{La}_{0.22})_2\text{O}_2\text{MnSe}_2$ is shown in Figure 13. Two separate views are shown in the figure to show the relations between magnetic moments of Mn^{2+} and Ce^{3+} (the vectors are not scaled). Mn^{2+} shows antiferromagnetic (AFM) ordering with moments orientated perpendicular to the $[\text{MnSe}_2]^{2-}$ plane. Mn^{2+} spins in adjacent layers at a given value of x are arranged antiferromagnetically. Nearest neighbour Mn-Mn interactions are antiferromagnetic as observed for a range of Mn_2X_2 tetrahedral systems⁴⁹ as are next-nearest-neighbour corner-shared interactions. A similar Mn^{2+} AFM ordering pattern was observed in $\text{A}_2\text{Mn}_3\text{Se}_4$ ($\text{A} = \text{Cs}, \text{Rb}$)^{50,51} systems. Ce^{3+} moments are aligned in the ab plane as typically observed in $\text{Ce}_2\text{O}_2^{2+}$ containing systems, and attributed to the single-ion anisotropy of Ce^{3+} . Within the plane the Ce moment direction seems principally controlled by the ordering of neighbouring MnSe_4 sites and follows the pattern of corner- and edge-sharing tetrahedra. Each Ce^{3+} moment lies parallel to the nearest Mn-Mn vector and is therefore parallel to or at 45° to the nuclear a axis depending on whether it lies close to an edge- (0°) or corner- (45°) sharing pair. The Ce moment direction observed is counter-intuitive based on the local Mn field, but alternate moment directions gave a significantly worse fit to the data. The 30 K magnetic moments of Ce^{3+} and Mn^{2+} are $0.85(1)$ and $4.12(1) \mu_B$, respectively. The low temperature Ce moment is comparable to that in $\text{Ce}_2\text{O}_2\text{FeSe}_2$ ^{25,48} and CeOMnAs ^{49,52}. We note that there is no evidence for Mn spin reorientation accompanying Ce ordering as observed for CeOMnAs ^{49,52,53} and similar systems.

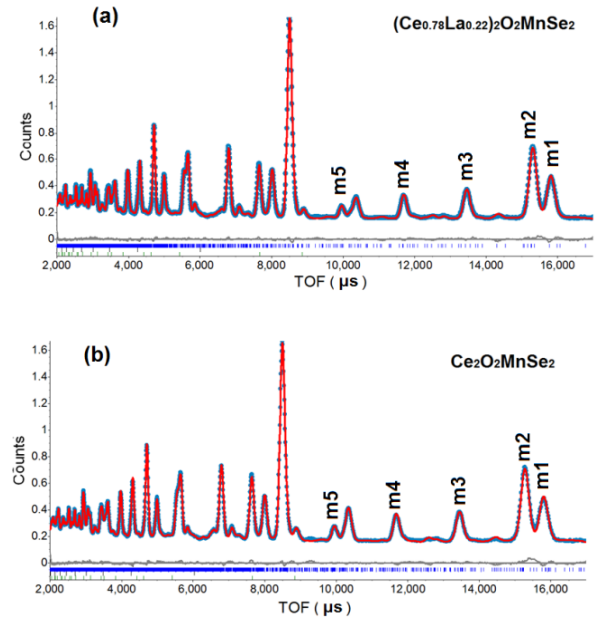
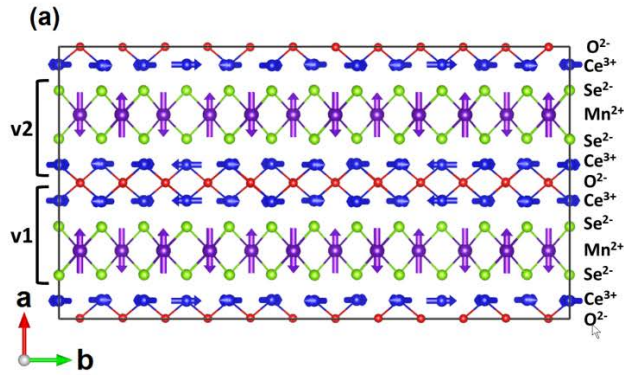


Figure 12. Rietveld refinement profiles (PND-bank3, 30K) of $(\text{Ce}_{0.78}\text{La}_{0.22})_2\text{O}_2\text{MnSe}_2$ and $\text{Ce}_2\text{O}_2\text{MnSe}_2$ magnetic structures. Dots: observed; solid line: calculated curve; grey line below:



difference curve; vertical tick marks: peak positions. m1 - m5 are the five magnetic peaks integrated in Figure 11.

Figure 13. Magnetic ordering pattern of $(\text{Ce}_{0.78}\text{La}_{0.22})_2\text{O}_2\text{MnSe}_2$ at 30 K. (a) View along c axis; (b) View along a axis of two sections ranged by v_1 and v_2 in (a) to show the moment relation between Ce^{3+} and Mn^{2+} . Note that axes are different to the nuclear cell. Some atoms are hidden and moment magnitude is not scaled. In (b), the arrows show moments of Ce^{3+} , MnSe_4 tetrahedra are given as shadowed blocks, 'x' indicates Mn^{2+} moments pointing down through the plane of the paper and '•' moments pointing up.

The temperature dependence of the magnetic moment (M) of Ce^{3+} and Mn^{2+} in $(\text{Ce}_{0.78}\text{La}_{0.22})_2\text{O}_2\text{MnSe}_2$ at different temperatures was extracted by combined refinement of all temperature-dependent PND data (six banks) and is plotted in Figure 14. Mn^{2+} shows AFM ordering at temperature below ~ 150 K and the moment saturates at $T < \sim 40$ K. Ce^{3+} shows magnetic ordering from $T < \sim 70$ K. As observed in related systems, the Ce ordering temperature is significantly higher than expected in a Ce ion only material, suggesting it is induced by Mn order.

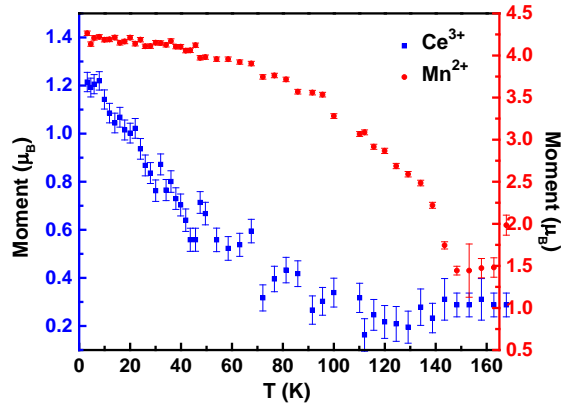


Figure 14. Magnetic moment of Ce^{3+} and Mn^{2+} in $(\text{Ce}_{0.78}\text{La}_{0.22})_2\text{O}_2\text{MnSe}_2$ at different temperatures.

Low temperature magnetic structure of $\text{Ce}_2\text{O}_2\text{MnSe}_2$. To understand the low temperature magnetic structure of incommensurate $\text{Ce}_2\text{O}_2\text{MnSe}_2$, we used the $Imcb$ supercell model to describe the nuclear structure. The magnetic structure can then be described by ordering at the Γ (o o o) point of the supercell model with irreducible representation $m\Gamma_4^{-33}$. The magnetic structure is therefore similar to

$(\text{Ce}_{0.78}\text{La}_{0.22})_2\text{O}_2\text{MnSe}_2$ with antiferromagnetic alignment of adjacent Mn^{2+} moments. During magnetic refinements, the fractional coordinates of atoms were fixed to RT values to prevent over parameterisation of the data and equivalent moment constraints were applied as for $(\text{Ce}_{0.78}\text{La}_{0.22})_2\text{O}_2\text{MnSe}_2$. The Rietveld profile of 30K PND_bank3 data for $\text{Ce}_2\text{O}_2\text{MnSe}_2$ is shown in Figure 12(b) and the profiles of PND bank1 - bank5 are shown in Figure S15. The final model gave refined moments of 0.82(2) and 4.14(1) μ_B on Ce^{3+} and Mn^{2+} sites. Mn again shows antiferromagnetic ordering with moments perpendicular to the nuclear ab plane; Ce moments again lie in the ab plane and follow the nearest Mn-Mn vector. Given the low number of magnetic observations local deviation from this simple model were not investigated.

Magnetic properties. $\text{Ce}_2\text{O}_2\text{MnSe}_2$ showed a linear dependence of magnetisation on field at 5 and 300 K (see Figure S16) with no hysteresis, indicating that the sample was free from significant ferromagnetic impurities. The temperature-dependent molar magnetic susceptibilities (χ_{mol}) of $\text{Ce}_2\text{O}_2\text{MnSe}_2$ and $(\text{Ce}_{0.78}\text{La}_{0.22})_2\text{O}_2\text{MnSe}_2$ are shown in Figure 15. χ_{mol} increases as the temperature is lowered, reaching a maximum at $T_m \approx 10$ K before increasing steeply below ~ 7 K. We attribute the low temperature increase to the MnSe_3^6 impurity observed in the PND. No significant anomaly is observed in the susceptibility data (or its first derivative) at the 150 K ordering temperature of Mn. This is presumably due to the persistence of significant short range 2-dimensional order above $T_N(\text{Mn})$, as evidenced by the broad peaks observed in the diffraction data of Figure 11(a) above this temperature. Similar observations have been made for CeOMnAs^{52} . The room temperature effective magnetic moment of $\mu_{\text{eff}} \sim 5 \mu_B$ is lower than would be expected for independent spins ($6.92 \mu_B$) again indicative of

ⁱⁱ All the magnetic structure information can be found as CIF files in the supporting information.

short range antiferromagnetic interactions. μ_{eff} decreases significantly at low temperature as Mn and Ce moments order. A decrease in susceptibility versus temperature was also observed for CeOMnAs around 10 K^{52,53} and was attributed⁵² to a departure from co-linearity of Ce and Mn moments in the *ab* plane at low temperatures. We see no anomalies in susceptibility to suggest reorientation of Mn moments, consistent with our neutron diffraction data.

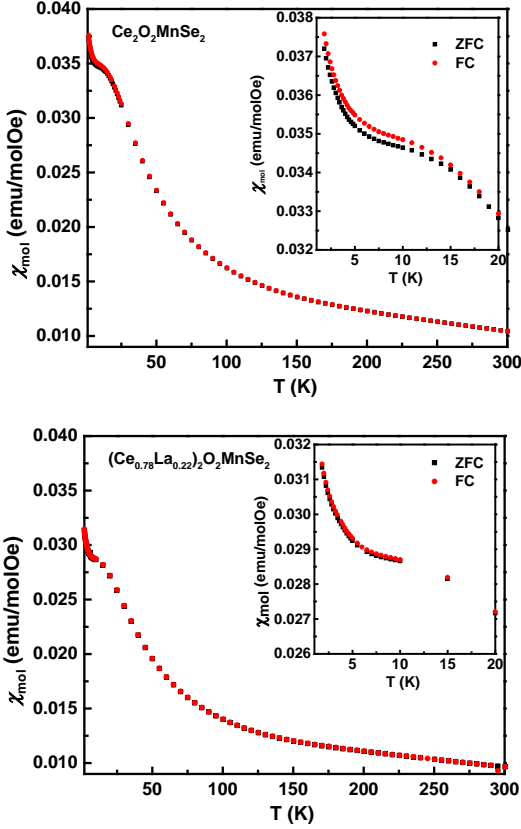


Figure 15. Molar magnetic susceptibility (χ_{mol}) of $\text{Ce}_2\text{O}_2\text{MnSe}_2$ and $(\text{Ce}_{0.78}\text{La}_{0.22})_2\text{O}_2\text{MnSe}_2$. Inset shows a zoom of the region from 1 K to 20 K.

Thermal expansion of $\text{Ce}_2\text{O}_2\text{MnSe}_2$. Variable temperature powder diffraction measurements were recorded for $\text{Ce}_2\text{O}_2\text{MnSe}_2$ to investigate thermal expansion properties and probe for possible phase transition beyond the magnetic ordering. Approximately 170 data sets recorded between 13 and 300 K were analysed. The cell parameters of $\text{Ce}_2\text{O}_2\text{MnSe}_2$ from 13 - 300 K are plotted in Figure 16 (a) and Figure S17. No evidence of structural phase transitions was observed. The volume coefficient of expansion was $2.865(1) \times 10^{-5} \text{ K}^{-1}$ from 13 to 300 K. The cell parameters can be described by a single term Einstein-type expression⁵⁴,

$$\ln\left(\frac{x}{x_0}\right) = \frac{C\theta}{\exp\left(\frac{\theta}{T}\right) - 1} \quad (1)$$

where T is temperature; x and x_0 are the cell parameters at T and 0 K, C a constant and θ the Einstein temperature. The fitted 0 K cell parameters are $a_0 = 5.6669(2) \text{ \AA}$, $b_0 = 5.6655(2) \text{ \AA}$, $c_0 = 9.0677(3) \text{ \AA}$, $V_0 = 291.13(1) \text{ \AA}^3$ and constants are $C_a = 1.02(3) \times 10^{-5} \text{ K}^{-1}$, $C_b = 0.96(3) \times 10^{-5} \text{ K}^{-1}$, $C_c = 1.88(3) \times 10^{-5} \text{ K}^{-1}$,

$C_V = 3.86(1) \times 10^{-5} \text{ K}^{-1}$ using a single Einstein temperature of 200(1) K. The modulation vector α remains essentially unchanged from 13 - 300 K as shown in Figure 16(b).

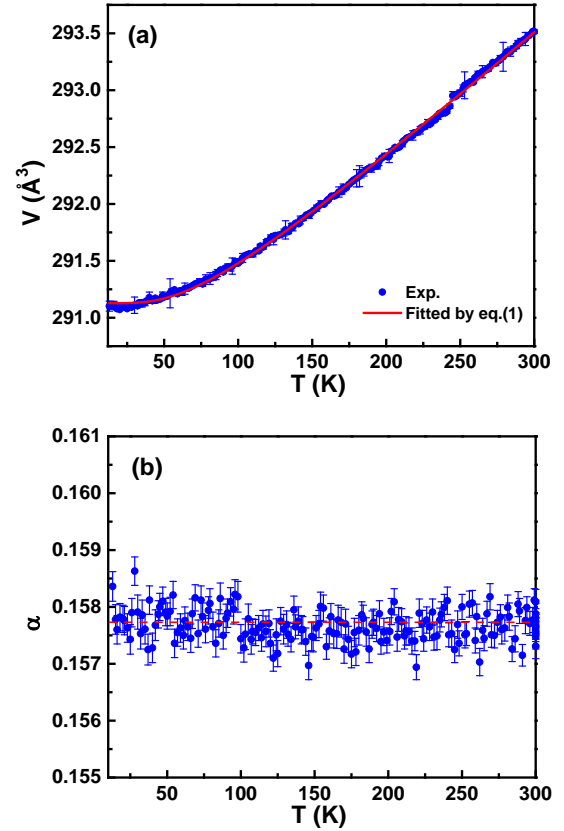


Figure 16. Temperature-dependent cell volume and independent modulation vector α of $\text{Ce}_2\text{O}_2\text{MnSe}_2$.

Conductivity properties. A typical $Z'-Z''$ impedance plot (RT) for $\text{Ce}_2\text{O}_2\text{MnSe}_2$ is given in Figure S18. From the permittivity, the response from grain (G) and grain boundary (GB) for the sample was assigned and their resistances were read from the $Z'-f$ data. The bulk conductivity (σ) Arrhenius plot of a $\text{Ce}_2\text{O}_2\text{MnSe}_2$ pellet is shown in Figure 17. The activation energy for charge carrier migration in the grain and grain boundary is 0.41(1) and 0.37(1) eV, respectively. At 24 °C, the grain conductivity σ_G is $\sim 9 \times 10^{-6} \Omega^{-1} \text{ cm}^{-1}$ and at 170 °C, σ_G increases to $\sim 7 \times 10^{-4} \Omega^{-1} \text{ cm}^{-1}$.

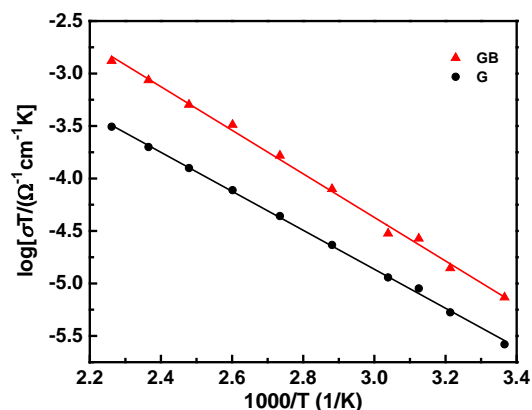


Figure 17. Arrhenius plots for the bulk conductivity σ of the $\text{Ce}_2\text{O}_2\text{MnSe}_2$ pellet. G: grain; GB: grain boundary.

CONCLUSIONS

Layered oxychalcogenide $(\text{Ce}_{1-x}\text{La}_x)_2\text{O}_2\text{MnSe}_2$ ($x = 0 - 0.7$) samples were prepared by solid state reactions and their crystal structures were determined using XRD and PND data. They show a $(3 + 1)$ D modulated structure with the superspace group $Cmme(\alpha_0^1)oso$ [67.12]. In $\text{Ce}_2\text{O}_2\text{MnSe}_2$, $\alpha = 0.158(1) \approx 3/19$ and can be varied by partially substituting Ce^{3+} for larger La^{3+} . A simple commensurate case $(\text{Ce}_{0.78}\text{La}_{0.22})_2\text{O}_2\text{MnSe}_2$ with $\alpha \approx 1/6$ was obtained. The structure description using a modulated approach is reported for $\text{Ce}_2\text{O}_2\text{MnSe}_2$ and $(\text{Ce}_{0.78}\text{La}_{0.22})_2\text{O}_2\text{MnSe}_2$, and the source of modulation in terms of the relative sizes of $[\text{Ce}_2\text{O}_2]^{2+}$ and $[\text{MnSe}_2]^{2-}$ layers identified. We identify M site ordering changes as a key mechanism for strain relief in these materials. The 3D structures of all $\text{Ln}_2\text{O}_2\text{MSe}_2$ materials reported to date can be described using a single superspace approach and differ in the ratio of corner- to edge-sharing tetrahedral groups they contain. In $(\text{Ce}_{0.78}\text{La}_{0.22})_2\text{O}_2\text{MnSe}_2$, Mn^{2+} shows antiferromagnetic ordering at temperatures lower than ~ 150 K and Ce^{3+} shows magnetic ordering at temperature lower than ~ 70 K. The magnetic structures of $(\text{Ce}_{0.78}\text{La}_{0.22})_2\text{O}_2\text{MnSe}_2$ and $\text{Ce}_2\text{O}_2\text{MnSe}_2$ at 30K were obtained from neutron diffraction data. The Mn^{2+} shows antiferromagnetic (AFM) ordering with moments perpendicular to the $[\text{MnSe}_2]$ plane and Ce^{3+} shows wave-like magnetic ordering with moments in the $[\text{Ce}_2\text{O}_2]$ plane. The conductivity of $\text{Ce}_2\text{O}_2\text{MnSe}_2$ pellet was also investigated from RT to 170 °C. The activation energy of charge carrier in the grain and grain boundary of the pellet is 0.41(1) and 0.37(1) eV, respectively.

ASSOCIATED CONTENT

Supporting Information. All SI figures, tables and cif files can be found in supporting information. This material is available free of charge via the Internet at <http://pubs.acs.org>.

AUTHOR INFORMATION

Corresponding Author

* John SO Evans, email: john.evans@durham.ac.uk

Author Contributions

All authors have given approval to the final version of the manuscript.

Funding Sources

This work was funded by the EPSRC under EP/J011533/1.

ACKNOWLEDGMENT

The authors thank ISIS for neutron diffraction measurements. The authors are extremely grateful to Dr. Dmitry S. Yufit for assistance with single crystal XRD measurement, Dr. Budhika Mendis for assistance during electron diffraction measurements, Mr. Leon Bowen for assistance with SEM measurements and Dr. Johan Buurma for SQUID measurements. We thank Prof. Shiv Halasyamani and Dr. ThanhThao Tran from the Department of Chemistry at the University of Houston for the SHG measurements. JSOE and IRE thank ANSTO for visiting research positions during which part of this paper was written.

REFERENCES

- (1) Imada, M.; Fujimori, A.; Tokura, Y. *Rev. Mod. Phys.* **1998**, *70*, 1039.
- (2) Stewart, G. R. *Rev. Mod. Phys.* **2011**, *83*, 1589.
- (3) Dagotto, E. *Rev. Mod. Phys.* **2013**, *85*, 849.
- (4) Battle, P. D.; Green, M. A.; Laskey, N. S.; Millburn, J. E.; Murphy, L.; Rosseinsky, M. J.; Sullivan, S. P.; Vente, J. F. *Chem. Mater.* **1997**, *9*, 552.
- (5) Masset, A. C.; Michel, C.; Maignan, A.; Hervieu, M.; Toulemonde, O.; Studer, F.; Raveau, B.; Hejtmanek, J. *Phys. Rev. B* **2000**, *62*, 166.
- (6) Amow, G.; Skinner, S. J. *J. Solid State Electr* **2006**, *10*, 538.
- (7) Tarancon, A.; Burriel, M.; Santiso, J.; Skinner, S. J.; Kilner, J. A. *J. Mater. Chem.* **2010**, *20*, 3799.
- (8) Uma, S.; Raju, A. R.; Gopalakrishnan, J. *J. Mater. Chem.* **1993**, *3*, 709.
- (9) Yashima, M.; Enoki, M.; Wakita, T.; Ali, R.; Matsushita, Y.; Izumi, F.; Ishihara, T. *J. Am. Chem. Soc.* **2008**, *130*, 2762.
- (10) Richard, A. P.; Russell, J. A.; Zakutayev, A.; Zakharov, L. N.; Keszler, D. A.; Tate, J. *J. Solid State Chem.* **2012**, *187*, 15.
- (11) Barreteau, C.; Pan, L.; Amzallag, E.; Zhao, L. D.; Berardan, D.; Dragoe, N. *Semicond. Sci. Tech.* **2014**, *29*, 064001.
- (12) Ohta, H.; Sugiura, K.; Koumoto, K. *Inorg. Chem.* **2008**, *47*, 8429.
- (13) Terasaki, I.; Sasago, Y.; Uchinokura, K. *Phys. Rev. B* **1997**, *56*, 12685.
- (14) Clarke, S. J.; Adamson, P.; Herkelrath, S. J. C.; Rutt, O. J.; Parker, D. R.; Pitcher, M. J.; Smura, C. F. *Inorg. Chem.* **2008**, *47*, 8473.
- (15) Kamihara, Y.; Watanabe, T.; Hirano, M.; Hosono, H. *J. Am. Chem. Soc.* **2008**, *130*, 3296.
- (16) Hiramatsu, H.; Ueda, K.; Takafuji, K.; Ohta, H.; Hirano, M.; Kamiya, T.; Hosono, H. *J. Appl. Phys.* **2003**, *94*, 5805.
- (17) Hiramatsu, H.; Ueda, K.; Takafuji, K.; Ohta, H.; Hirano, M.; Kamiya, T.; Hosono, H. *J. Mater. Res.* **2004**, *19*, 2137.
- (18) Ueda, K.; Takafuji, K.; Hiramatsu, H.; Ohta, H.; Kamiya, T.; Hirano, M.; Hosono, H. *Chem. Mater.* **2003**, *15*, 3692.
- (19) Ueda, K.; Takafuji, K.; Hosono, H. *J. Solid State Chem.* **2003**, *170*, 182.
- (20) Ueda, K.; Takafuji, K.; Yanagi, H.; Kamiya, T.; Hosono, H.; Hiramatsu, H.; Hirano, M.; Hamada, N. *J. Appl. Phys.* **2007**, *102*, 113714.
- (21) Ijjaali, I.; Mitchell, K.; Haynes, C. L.; McFarland, A. D.; Van Duyne, R. P.; Ibers, J. A. *J. Solid State Chem.* **2003**, *176*, 170.

- (22) Hiramatsu, H.; Ueda, K.; Kamiya, T.; Ohta, H.; Hirano, M.; Hosono, H. *J. Phys. Chem. B* **2004**, *108*, 17344.
- (23) Hiramatsu, H.; Ueda, K.; Kamiya, T.; Ohta, H.; Hirano, M.; Hosono, H. *J. Mater. Chem.* **2004**, *14*, 2946.
- (24) Baranov, I. Y.; Dolgikh, V. A.; Popovkin, B. A. *Zhurnal Neorganicheskoi Khimii* **1996**, *41*, 1916.
- (25) McCabe, E. E.; Free, D. G.; Evans, J. S. O. *Chem. Commun.* **2011**, *47*, 1261.
- (26) Nitsche, F.; Niklaus, R.; Johrendt, D. *Z. Anorg. Allg. Chem.* **2014**, *640*, 2897.
- (27) Tuxworth, A. J.; McCabe, E. E.; Free, D. G.; Clark, S. J.; Evans, J. S. O. *Inorg. Chem.* **2013**, *52*, 2078.
- (28) Ainsworth, C. M.; Wang, C.-H.; Tucker, M. G.; Evans, J. S. O. *Inorg. Chem.*, **2015**, *54*, 1563.
- (29) Petricek, V.; Dusek, M.; Palatinus, L. *Z. Kristallogr.* **2014**, *229*, 345.
- (30) Palatinus, L. *Acta Crystallogr. A* **2004**, *60*, 604.
- (31) Orlov, I.; Palatinus, L.; Chapuis, G. *J. Appl. Crystallogr.* **2008**, *41*, 1182.
- (32) Coelho, A. A.; Evans, J. S. O.; Evans, I. R.; Kern, A.; Parsons, S. *Powder Diffr.* **2011**, *26*, S22.
- (33) Campbell, B. J.; Stokes, H. T.; Tanner, D. E.; Hatch, D. M. *J. Appl. Crystallogr.* **2006**, *39*, 607.
- (34) Brown, P. J. In *International tables for crystallography*; 3 ed.; Prince, E., Ed. 2004; Vol. C, p 454.
- (35) Freeman, A. J.; Desclaux, J. P. *J. Magn. Magn. Mater.* **1979**, *12*, 11.
- (36) D'Sa, J.; Bhoje, P. A.; Priolkar, K. R.; Das, A.; Krishna, P. S. R.; Sarode, P. R.; Prabhu, R. B. *Pramana-j. Phys.* **2004**, *63*, 227.
- (37) Jacobson, A. J.; Fender, B. E. F. *J. Chem. Phys.* **1970**, *52*, 4563.
- (38) Pollard, R. J.; McCann, V. H.; Ward, J. B. *Journal of Physics C-Solid State Physics* **1983**, *16*, 345.
- (39) Ok, K. M.; Chi, E. O.; Halasyamani, P. S. *Chem. Soc. Rev.* **2006**, *35*, 710.
- (40) McCabe, E. E.; Free, D. G.; Mendis, B. G.; Higgins, J. S.; Evans, J. S. O. *Chem. Mater.* **2010**, *22*, 6171.
- (41) Stokes, H. T.; Campbell, B. J.; Hatch, D. M. *Acta Crystallogr. A* **2007**, *63*, 365.
- (42) Janssen, T.; Janner, A.; Looijenga-Vos, A.; Wolff, P. M. d. In *International Tables for Crystallography* 2006; Vol. C, p 907.
- (43) van Smaalen, S. *Incommensurate Crystallography*; Oxford University Press: Oxford, 2007.
- (44) Strobel, S.; Choudhury, A.; Dorhout, P. K.; Lipp, C.; Schleid, T. *Inorg. Chem.* **2008**, *47*, 4936.
- (45) Baroni, D. A. *Zeitschrift für Kristallographie - Crystalline Materials* **1938**, *99*, 336.
- (46) Berger, R.; Van Bruggen, C. F. *Journal of the Less Common Metals* **1985**, *113*, 291.
- (47) Shannon, R. D. *Acta Crystallogr. A* **1976**, *32*, 751.
- (48) McCabe, E. E.; Stock, C.; Bettis, J. L., Jr.; Whangbo, M. H.; Evans, J. S. O. *Phys. Rev. B* **2014**, *90*, 235115.
- (49) Corkett, A. J.; Free, D. G.; Clarke, S. J. *Inorg. Chem.* **2014**, DOI:10.1021/ic5026608.
- (50) Bronger, W.; Hardtdegen, H.; Kanert, M.; Müller, P.; Schmitz, D. *Z. Anorg. Allg. Chem.* **1996**, *622*, 313.
- (51) Bronger, W.; Müller, P. *J. Alloy. Compd.* **1997**, *246*, 27.
- (52) Zhang, Q.; Tian, W.; Peterson, S. G.; Dennis, K. W.; Vahnin, D. *arXiv:1411.3380v1* **2014**.
- (53) Tsukamoto, Y.; Okamoto, Y.; Matsuhira, K.; Whangbo, M.-H.; Hiroi, Z. *J. Phys. Soc. Jpn.* **2011**, *80*, 094708.
- (54) Reeber, R. R. *physica status solidi (a)* **1975**, *32*, 321.

